Remote Sensing of Environment 186 (2016) 32–46

Contents lists available at ScienceDirect

Remote Sensing of Environment

journal homepage: www.elsevier.com/locate/rse

Estimating Arctic sea-ice shortwave albedo from MODIS data

Ying Qu [a], Shunlin Liang [b,c,d,*], Qiang Liu [c,e], Xijia Li [a], Youbin Feng [c,e], Suhong Liu [b,c]

[a] School of Geographical Sciences, Northeast Normal University, Changchun 130024, China
[b] School of Geography, Beijing Normal University, Beijing 100875, China
[c] State Key Laboratory of Remote Sensing Science, Beijing Normal University, Beijing 100875, China
[d] Department of Geographical Sciences, University of Maryland, College Park 20742, MD, USA
[e] College of Global Change and Earth System Science, Beijing Normal University, Beijing 100875, China

ARTICLE INFO

Article history:
Received 11 November 2015
Received in revised form 30 July 2016
Accepted 10 August 2016
Available online 19 August 2016

Keywords:
Arctic
Albedo
Sea ice
Direct-estimation algorithm
MODIS

ABSTRACT

Shortwave surface albedo of the Arctic sea-ice zone is one of the most important parameters in the surface energy budget over the northern hemispheric cryosphere. Although many global and regional broadband surface albedo products have been generated from satellite observations, most of them contain albedo over land-surfaces only, and the albedo over ocean and sea-ice surfaces is usually left blank or estimated based on the lambertian-assumption. In this paper, we extend the BRDF-based direct-estimation algorithm for mapping the shortwave surface albedo of the Arctic sea-ice zone with Moderate Resolution Imaging Spectroradiometer (MODIS) data. Firstly, a bidirectional reflectance distribution function (BRDF) database for sea ice was generated based on simulations of the asymptotic radiative transfer (ART) and the three components ocean water albedo (TCOWA) model. Secondly, a linear regression relationship between top of atmosphere (TOA) reflectance and surface broadband albedo was developed for different angular bins. Finally, the direct-estimation coefficients derived by the angular bin regression were stored in a pre-calculated look up table (LUT). When the MODIS L1B swath data are available, the corresponding coefficients are searched based on the solar/view geometry. Therefore, the shortwave surface albedo can be estimated from single-angular observations. Compared with the in situ measurements from the Tara polar ocean expedition in 2007, the results indicate that the albedo estimated by the BRDF-based direct-estimation algorithm has an R^2 value of 0.67 and root mean square error (RMSE) of 0.068. The validation results show that the BRDF-based direct-estimation algorithm is suitable for mapping shortwave surface albedo of the Arctic sea-ice zone, which corrects the reflectance anisotropic effect with prior physical BRDF database and makes it possible to generate long-term Arctic surface albedo products with higher spatial and temporal resolutions.

1. Introduction

Shortwave surface albedo of the Arctic sea-ice zone is an important parameter in the surface energy budget over the northern hemispheric cryosphere (Hall, 2004; Perovich et al., 2007; Cao et al., 2015), which affects the solar heat input, separation, and reallocations among the earth-atmosphere system (Trenberth et al., 2009).

As one of the most sensitive regions to the effects of global warming, the Arctic sea-ice zone is profoundly affected by the changing climate (Fyfe et al., 1999; Johannessen et al., 2004; Post and Palkovacs, 2009). There is evidence that the extent of Arctic sea ice in summer has been decreasing over the past 30 years (Serreze et al., 2007; Stroeve et al., 2007, 2012), and Arctic sea ice is becoming thinner (Kwok and Rothrock, 2009) and darker (Riihelä et al., 2013a). Because of the high reflectivity of snow and ice surfaces, surface albedo of the Arctic increases/decreases significantly as the sea ice freezes/melts seasonally (Perovich et al., 2002). Against the background of global warming, the decrease of surface albedo in the Arctic sea-ice zone leads to an increase of solar heat input to the sea ice and ocean water (Perovich et al., 2007). The so-called sea-ice albedo feedback mechanism (Curry et al., 1995; Hall and Qu, 2006) enhances the relationship between surface albedo and regional climate, which makes the surface albedo over the Arctic sea-ice zone a critical parameter in global climate models (GCMs) (Liu et al., 2007; Pedersen, 2007).

Satellite remote sensing is widely used for mapping the temporal and spatial variation of shortwave surface albedo (He et al., 2014; Liang et al., 2010; Qu et al., 2015). Several previous studies focus on mapping the broadband albedo of Arctic sea ice using Advanced Very High Resolution Radiometer (AVHRR) data (Comiso, 2001; De Abreu et al., 1994; Lindsay and Rothrock, 1994; Xiong et al., 2002). Several other studies for mapping Arctic surface or planetary albedo also include sea-ice albedo from operational AVHRR data (Knap and

* Corresponding author at: No. 19 Xinjiekouwai Street, Beijing Normal University, Beijing, China.
E-mail addresses: quy100@nenu.edu.cn (Y. Qu), sliang@bnu.edu.cn (S. Liang).

http://dx.doi.org/10.1016/j.rse.2016.08.015
0034-4257/

Table 1
Current available broadband albedo products over the Arctic region.

Name	Spatial resolution	Temporal resolution	Temporal span	Spatial coverage	Sensors	Albedo quantity	References
APP	5 km	Twice-daily	1981–2005	Arctic/Antarctic	AVHRR	Black-sky albedo	Key et al. (2001)
APP-x	25 km	Monthly	1982–present	Arctic/Antarctic	AVHRR	Black-sky albedo/white-sky albedo	Key et al. (2014) Wang and Key (2005)
CM-SAF SAL	15 km	Weekly/monthly	2004–present 2009–present	Baseline area/Arctic	AVHRR/SEVIRI	Black-sky albedo	Riihelä et al. (2010)
CLARA SAL	0.25° (global)/25 km (Arctic/Antarctic)	Pentad/monthly	1982–2009	Global/Arctic/Antarctic	AVHRR	Black-sky albedo	Riihelä et al. (2013b)

Oerlemans, 1996; Stroeve et al., 1997) and AVHRR pathfinder data (Key et al., 2001; Laine, 2004; Stroeve et al., 2001). In addition, a method for deriving gap-free shortwave surface albedo with passive microwave data has also been developed (Laine et al., 2014, 2011).

In recent decades, many global and regional long-term albedo products have been derived by geostationary and polar-orbit satellite observations (Liang et al., 2010; Qu et al., 2015). However, most of these products contain albedo over the land-surface only, and the albedo over the Arctic sea ice region is usually left blank or estimated by the methods based on the Lambertian assumption. The following currently available surface albedo products (Table 1) include sea ice albedo: the AVHRR Polar Pathfinder (APP) albedo product (Key et al., 2001), the APP-extended (APP-x) albedo product (Key et al., 2014; Wang and Key, 2005), the Satellite Application Facility on Climate Monitoring (CM-SAF) surface albedo (SAL) product (Riihelä et al., 2010), and the CM-SAF cLouds, Albedo and RAdiation (CLARA) SAL product (Riihelä et al., 2013b).

Although encouraging achievements of remote sensing of snow/sea-ice surface albedo have been obtained, the consideration of reflectance anisotropy in the former products still needs to be improved. The widely used lambertian-based method ignored the reflectance anisotropy of snow and ice surfaces, and treated the sea ice as lambertian or corrected the reflectance with simple anisotropy coefficients. However, the snow and sea ice surfaces cannot be considered as lambertian. The field measurements of directional and spectral reflectance over snow surface (Bourgeois et al., 2006; Peltoniemi et al., 2005) show that the anisotropy of snow is highly variable by solar/view geometries, wavelength, and snow wetness. The anisotropy effect of old wet snow can be ignored, however the anisotropy effect of fresh and dry snow cannot be ignored due to its strong forward-scattering (Dumont et al., 2010; Wu et al., 2012). In addition, the spatial and temporal resolutions of the currently available broadband surface albedo products of the Arctic sea-ice zone are relatively coarse, and products with finer spatial and temporal resolution are still required.

In this paper, we extend the BRDF-based direct-estimation algorithm for mapping the shortwave surface albedo of the Arctic sea-ice zone with Moderate Resolution Imaging Spectroradiometer (MODIS) data. In short, we propose a hybrid method, which incorporates physical model simulations and empirical regressions in different steps. Firstly, we build a bidirectional reflectance distribution function (BRDF) database for sea ice based on physical models of snow/ice and ocean water. Then, we establish a linear regression relationship between top of atmosphere (TOA) reflectance and surface broadband albedo among different angular bins. Finally, the BRDF-based direct-estimation coefficients derived in the regression step are stored in a pre-calculated look up table (LUT). When the MODIS L1B swath data are obtained, the corresponding coefficients are searched based on the solar/view geometry, therefore the shortwave surface albedo can be estimated from single-angular observations.

This paper is organized as follows. Firstly, we present the BRDF-based direct-estimation algorithm for mapping surface albedo over the Arctic sea-ice region in Section 2. The methodology for building the BRDF database, atmospheric radiative transfer simulations, and angular bin regression are also described in this section. We then provide a description for the direct-estimated result and validate it with the in situ measurements, and CLARA SAL product in Section 3. Finally, we present the primary conclusions for this paper in Section 4.

2. Methodology

2.1. Overall framework

The direct-estimation algorithm is a method for directly mapping broadband surface albedo from top of atmosphere (TOA) reflectance (Liang, 2003, Liang et al., 1999; Qu et al., 2014). Compared with algorithms based on multi-date/angular observations (Lucht et al., 2000; Schaaf et al., 2002), the direct-estimation algorithm enables estimates of broadband surface albedo with single-date/angular observations

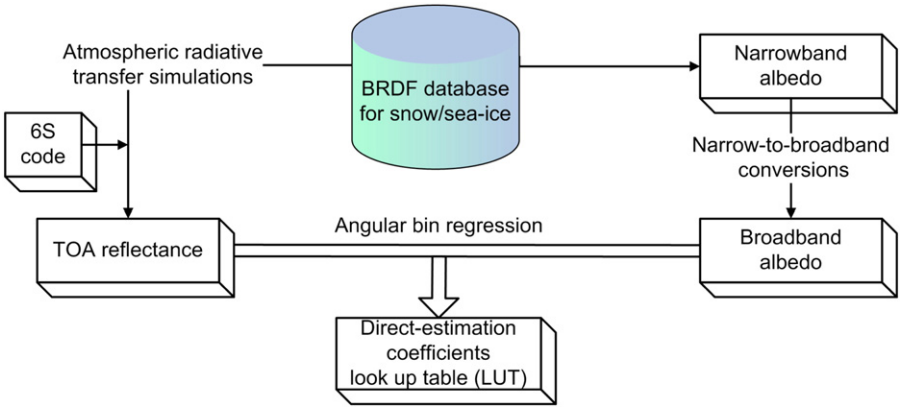

Fig. 1. Flow chart for deriving the direct-estimation coefficients.

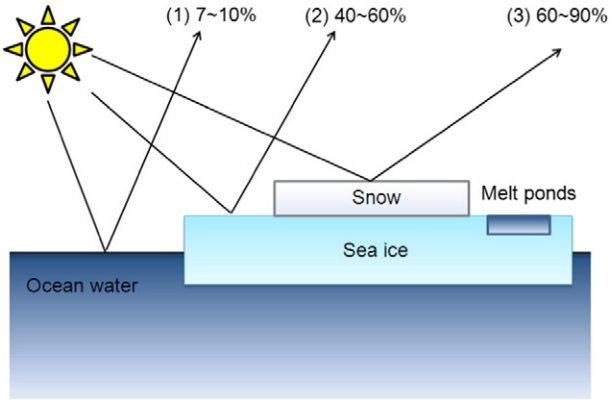

Fig. 2. The Arctic sea-ice zone is covered with bare sea-ice, snow covered sea-ice and ocean water.

and is more capable of characterizing the temporal variation of surface albedo, especially when the surface BRDF changes rapidly (Qu et al., 2014). The direct-estimation algorithm was first proposed with a lambertian spectral reflectance library based on neural network (NN) (Liang et al., 1999) and projection pursuit regression (PPR) (Liang, 2003) methods. In a consequent study, Liang et al. (2005) used a Discrete-Ordinate Radiative Transfer (DISORT) model (Stamnes et al., 1988) for simulating surface BRDF of snow/ice and applied an angular bin regression for estimating broadband surface albedo over the Greenland ice sheet. Recently, the BRDF database of the direct-estimation algorithm was further improved by the MODIS (Wang et al., 2013) and Polarization and Directionality of the Earth's Reflectances (POLDER) (Qu et al., 2014) BRDF databases.

The concept of the BRDF-based direct-estimation algorithm is to develop a relationship between broadband surface albedo and TOA reflectance over sea ice surfaces based on a priori BRDF database. The coefficients for converting TOA reflectance to broadband surface albedo with different solar/view geometry are pre-calculated and stored in look up tables (LUTs).

The direct-estimation coefficients are derived by the following steps (Fig. 1): (1) A surface BRDF database for sea-ice is built for deriving the training dataset (directional TOA reflectance and its corresponding surface broadband albedo); (2) The narrowband and broadband albedo are derived based on the surface BRDF database; (3) The TOA reflectance is derived from the atmospheric radiative transfer simulations; (4) The relationships between TOA reflectance and surface broadband albedo at each solar/viewing angular bin are developed, from which the direct-estimation coefficients are obtained. The direct-estimation coefficients can be directly used for estimating surface broadband albedo. These main steps for deriving the direct-estimation coefficients are described in the following sub-sections in details.

2.2. BRDF database for sea ice

The Arctic sea-ice zone is seasonally covered with bare sea-ice, snow-covered sea-ice, melt ponds and open ocean water. For simplicity, we assume that a pixel in satellite image of Arctic sea-ice zone can be considered as linear combination of snow, ice, and ocean water (Fig. 2). In this study, the reflectance of melt ponds is also considered as linear mixing of the reflectance signatures of snow, ice, and ocean water. A sea-ice BRDF database with varied snow/ice optical properties and covered fractions is built for representing different snow/ice types and sea-ice/ocean water mixed sceneries.

The sea-ice BRDF database is derived by linear mixing of the BRDF over snow, ice and ocean water surfaces (Fig. 3),

$$BRDF_{sea\ \ ice} = f_{snow} \times BRDF_{snow} + f_{ice} \times BRDF_{ice} + f_{ocean} \times BRDF_{ocean}, \quad (1)$$

where $BRDF_{sea\ \ ice}$ is the sea-ice BRDF dataset, $BRDF_{snow}$, $BRDF_{ice}$ and $BRDF_{ocean}$ are the BRDF over snow, ice, and ocean water surfaces, respectively. The f_{snow}, f_{ice} and f_{ocean} are the fractions of snow, ice and ocean water ($f_{snow}+f_{ice}+f_{ocean}=1$), which are used for representing the scenarios of snow, ice and ocean water (or melt ponds) mixed with

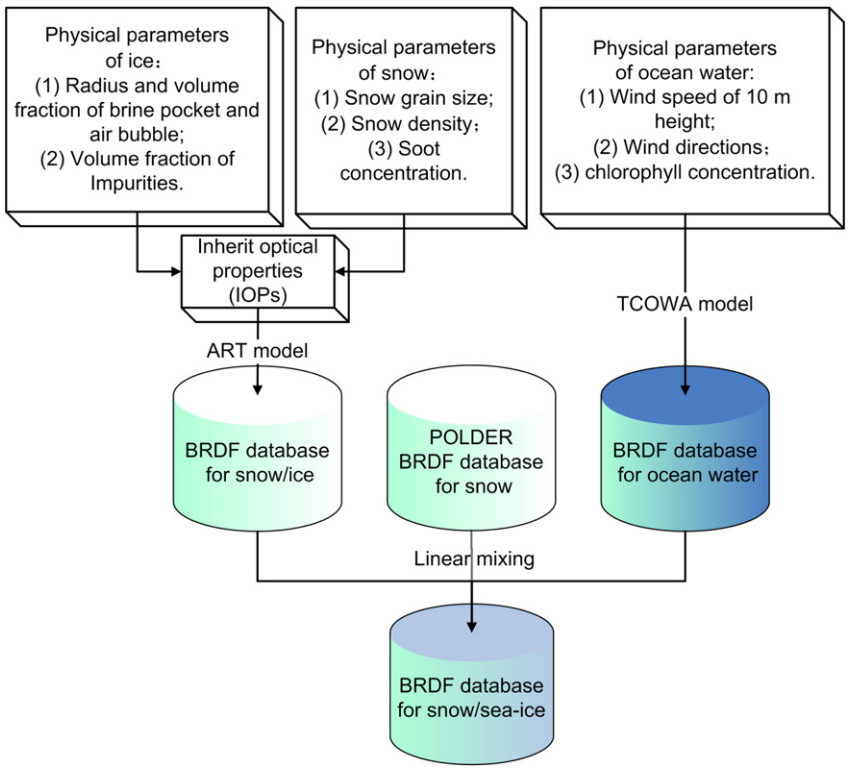

Fig. 3. Flow chart for deriving the surface BRDF database of snow/sea-ice.

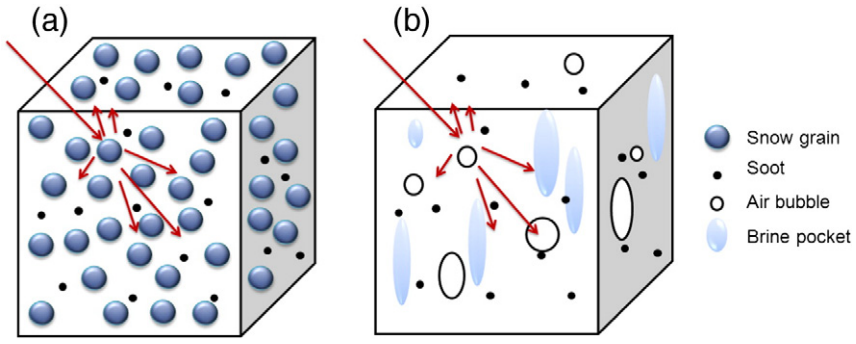

Fig. 4. A conceptual snow/ice model. (a) Snow; (b) ice.

different fractions. Considering the calculation efficiency, we use a Monte-Carlo method to simulate the BRDF database for sea ice, set the f_{snow}, f_{ice} and f_{ocean} as a random number from 0.00 to 1.00 by a pseudo-random number generator, and extract the snow, ice and ocean water BRDF data from their corresponding dataset randomly. Finally, a sea-ice BRDF database with 100,000 cases is derived by Eq. (1).

The BRDF databases for snow and ice are consist of the dataset derived by physical models and the POLDER snow BRDF database (Qu et al., 2014). In this study, the asymptotic radiative transfer (ART) model (Kokhanovsky and Zege, 1997, Kokhanovsky and Zege, 2004; Zege et al., 2011) is used for deriving the BRDF over snow and ice surfaces. In this model, the white-sky albedo (WSA) and black-sky albedo (BSA) of a semi-infinite layer can be calculated as

$$\alpha_{wsa} = \exp(-y) \tag{2}$$

$$\alpha_{bsa}(\theta_{bsa}) = \exp(-y\gamma(\theta_{bsa})), \tag{3}$$

where α_{wsa} and α_{bsa} are the white-sky albedo and black-sky albedo, respectively. The escape function $\gamma(\theta_{bsa})$ at zenith angle θ_{bsa} and the fraction of the absorbed light energy from a semi-infinite medium under diffuse illumination y are defined as

$$\gamma(\theta_{bsa}) = \frac{3}{7}(1 + 2\cos\theta_{bsa}) \tag{4}$$

$$y = 4\sqrt{\frac{\sigma_a}{3\sigma_e(1-g)}}, \tag{5}$$

where σ_a and σ_e are the absorption and extinction coefficients, respectively. g denotes the asymmetry parameter of the medium. The inherit optical properties (IOPs) of snow/ice (σ_a, σ_e, and g) are calculated by an improved parameterization method (Stamnes et al., 2011) based on Mie theory. Compared with the former parameterization method (Hamre et al., 2004) which is only valid for wavelengths shorter than ~1.2 μm, the IOPs over the whole shortwave band can be accurate and quickly calculated by the improved parameterization method.

Table 2
Physical parameters of snow for calculating its IOPs.

Parameter	Symbol	Units	Value
Snow grain size	r_e	μm	50, 100, 200, 250, 500, 800, 1000, 1500, 2000
Snow density	ρ_s	g cm^{-3}	0.1, 0.2, 0.3, 0.4, 0.5
Soot concentrations	C_{soot}	ppmv	0, 0.01, 0.1, 0.3, 1, 5

According to the ART model, the BRDF of snow/ice is

$$BRDF_{snow/ice}(\theta_s, \theta_v, \varphi) = BRDF_0(\theta_s, \theta_v, \varphi) \times \exp\left[-y\frac{\gamma(\theta_s)\gamma(\theta_v)}{BRDF_0(\theta_s, \theta_v, \varphi)}\right], \tag{6}$$

where $BRDF_0(\theta_s,\theta_v,\varphi)$ is defined as the BRDF of a semi-infinite non-absorbing medium, which can be expressed as

$$BRDF_0(\theta_s, \theta_v, \varphi) = \frac{a + b(\cos\theta_s + \cos\theta_v) + c\cos\theta_s\cos\theta_v + p(\Theta)}{4(\cos\theta_s + \cos\theta_v)}, \tag{7}$$

where θ_s, θ_v, and φ are the solar zenith angle (SZA), view zenith angle (VZA), and relative azimuth angle (RAA), respectively, $a = 1.247$, $b = 1.186$, $c = 5.157$, and Θ is the scattering angle, which is given in degrees in the following equations. Θ and $p(\Theta)$ can be expressed as (Kokhanovsky et al., 2005)

$$\cos\Theta = -\cos\theta_v\cos\theta_s + \sin\theta_v\sin\theta_s\cos\varphi \tag{8}$$

$$p(\Theta) = 11.1 \times \exp(-0.087\Theta) + 1.1 \times \exp(-0.014\Theta), \tag{9}$$

The processes for deriving snow/ice surface BRDF can be separated into two steps (left branch of Fig. 3): (1) The IOPs of snow/ice are calculated for a variety of surface physical parameters; (2) The BRDF is simulated using the ART model. In the conceptual snow/sea-ice model, the snow consists of snow grains and soots impurities, while ice consists of brine pockets, air bubbles and soots (Fig. 4). The input physical parameters for snow/ice are snow grain size, density, volume of impurities/soot, radius and volume fraction of brine pockets and air bubbles) (Tables 2 and 3). The IOPs are first calculated by an improved parameterization method (Stamnes et al., 2011). (3) Then, the BRDF for snow/ice is derived from IOPs by Eq. (6).

The POLDER-3 surface BRDF database (http://postel.mediasfrance.org/en/BIOGEOPHYSICAL-PRODUCTS/BRDF) for snow is also employed for this study. This dataset is the unique available surface BRDF dataset at the scale of satellite pixels and can provide much more realistic information than physical simulations. Thus, this dataset is used for presenting the anisotropic reflectance signatures of snow-covered sceneries in this study, which is also considered as an important complementation of the simulations of ART model. In this database, multi-angular reflectance observations (80 to 500 angular samples for a pixel) are collected

Table 3
Physical parameters of ice for calculating its IOPs.

Parameter	Symbol	Units	Value
Brine pocket volume fraction	V_{br}	–	0.1, 0.15, 0.25, 0.5
Brine pocket radius	r_{br}	μm	200, 500, 1000
Air bubble volume fraction	V_{bu}	–	0.005, 0.01, 0.02, 0.05
Air bubble radius	r_{bu}	μm	100, 200, 500
Impurities volume fraction	C_{soot}	ppmv	0.1, 1, 5

Table 4
Physical parameters of case 1 ocean water.

Parameter	Symbol	Units	Value
Wind directions	phw	Degree	0, 75, 150, 225, 300
Wind speed of 10 height	wspd	m/s	0, 3, 6, 9, 12, 15, 18, 21, 24
Chlorophyll concentrations	chl	mg/m^3	0.03, 0.1, 0.3, 1.0, 3.0, 10

by accumulating one-month measurements from different satellite overpasses. The dataset is corrected for molecular and aerosols scattering, as well as atmospheric absorption (Leroy et al., 1997). In addition, we also performed a series of processes, such as quality control, landcover classification, band conversions and interpolation/extrapolation, to derive the final BRDF database for snow (627 samples of snow BRDF datasets are obtained). The method for processing the POLDER BRDF database has been described in our earlier paper (Qu et al., 2014) in detail.

The BRDF database for ocean water is generated by the three components ocean water albedo (TCOWA) model (Feng et al., 2016). The BRDF over ocean water surface is considered as the weighted sum of the three components (sun glint, whitecaps, and water-leaving reflectance from just beneath the air-water interface) (Sayer et al., 2010)

$$BRDF_{ocean} = W \times BRDF_{ef} + (1-W)\left(BRDF_g + BRDF_{wl}\right), \tag{10}$$

where $BRDF_{ocean}$ is the BRDF of ocean water, W is the whitecaps coverage which is a function of wind speed (Monahan and Muircheartaigh, 1980), and $BRDF_{ef}$, $BRDF_g$, and $BRDF_{wl}$ are the BRDF of the effective reflectance of total whitecaps, sun glints, and water-leaving terms, respectively. In the TCOWA model, the whitecap reflectance is simplified as Lambertian (Koepke, 1984), the sun glints reflectance is simulated by the Cox-Munk model (Cox and Munk, 1954), and the water-leaving reflectance of case 1 water (open ocean water) depends mainly on wavelength and pigment concentration (Morel and Maritorena, 2001) and weakly on solar/view geometry and wind field (Morel et al., 2002). Then, the black-sky albedo and white-sky albedo of ocean water surface can be derived by integration over angles and wavelengths. The BRDF simulated by the TCOWA model agrees well with field measured data, and has been used for generating an ocean albedo product with meteorological reanalysis data (Feng et al., 2016).

The BRDF of ocean water surface is simulated with following physical parameters: wind speed of 10 m height, wind directions, and chlorophyll concentrations (Table 4). Because the Arctic Ocean water can be considered as clean without suspending materials and sediments, only the BRDF of case 1 ocean water is simulated by TCOWA model (Eq. (10)).

2.3. Methods for deriving narrow and broad band albedo

The narrowband surface albedo can be calculated by integrating of the BRDF over all viewing zenith angles. The black-sky and white-sky albedo can be expressed as (e.g. Qu et al., 2015)

$$\alpha_{bsa}(i) = \int_0^{\frac{\pi}{2}}\int_0^{2\pi} BRDF_i(\theta_s,\theta_v,\varphi)d\theta_s d\varphi_s, \tag{11}$$

$$\alpha_{wsa}(i) = \int_0^{\frac{\pi}{2}}\int_0^{2\pi}\int_0^{\frac{\pi}{2}}\int_0^{2\pi} BRDF_i(\theta_s,\theta_v,\varphi)d\theta_s d\theta_v d\varphi_s d\varphi_v, \tag{12}$$

Table 6
Input parameters of 6S atmospheric radiative transfer simulations.

Parameters	Value
Atmospheric type	Arctic Summer, Arctic Winter
Aerosol type	Continental, maritime
AOD	0, 0.05, 0.1, 0.15, 0.2
Target altitude	0, 0.5, 1.0, 1.5, 2.0, 2.5, 3, 3.5 (km)
Solar zenith angle	0, 2, 4, …, 78, 80 (degree)
View zenith angle	0, 2, 4, …, 62, 64 (degree)
Relative azimuth angle	0, 5, 10, …, 175, 180 (degree)

where $\alpha_{bsa}(i)$ and $\alpha_{wsa}(i)$ is the black-sky and white-sky albedo of band i, respectively, and $BRDF_i(\theta_s,\theta_v,\varphi)$ is the BRDF of band i, when the solar zenith angle is θ_s, view zenith angle is θ_v, φ is the relative azimuth angle from the solar azimuth angle φ_s minus the view azimuth angle φ_v.

The broadband surface albedo is estimated by linear combinations of narrow band (spectral) albedo (Liang, 2001)

$$\alpha = c_0 + \sum_{i=1}^{n} c_i\alpha(i), \tag{13}$$

where α is the broadband (shortwave) surface albedo, $\alpha(i)$ is the narrowband albedo of MODIS band i ($i=1,2,\cdots,7$), and c_i are coefficients of the narrow-to-broadband conversions, which are listed in Table 5 (coefficients from Stroeve et al., 2005 are used for snow/ice surfaces).

The blue-sky albedo (instantaneous measured albedo) can be expressed as a linear combination of black and white-sky albedo (Lewis and Barnsley, 1994; Pinty et al., 2005; Román et al., 2010)

$$\alpha_{blue-sky} = \alpha_{bsa}\cdot(1-D) + \alpha_{wsa}\cdot D, \tag{14}$$

where $\alpha_{blue-sky}$ is the blue-sky albedo, α_{bsa} and α_{wsa} is black and white-sky albedo, respectively. D stands for the fraction of diffuse skylight, which varies with aerosol optical depth (AOD), solar zenith angle and wavelength. The fraction of skylight can be estimated by a look up table (LUT) based method (Strahler et al., 1999). Under clear-sky conditions, an empirical equation (Stokes and Schwartz, 1994) can be used for deriving the fraction of skylight in this study

$$D = 0.122 + 0.85e^{-4.8\cos(\theta_s)}, \tag{15}$$

where D is the fraction of diffuse skylight and θ_s is the solar zenith angle.

2.4. BRDF-based atmospheric radiative transfer simulations

In the atmospheric radiative transfer simulations process, we use a BRDF-based parameterization equation (Qin et al., 2001) which is also used in our related works (He et al., 2012; Qu et al., 2014; Wang et al., 2013). In the traditional studies, the TOA reflectance is usually simulated by inputting the surface BRDF data to the Second Simulation of the Satellite Signal in the Solar Spectrum (6S) code directly, which is limited by the low computational efficiency. Instead, the following approximate formula is used for simulating TOA reflectance by incorporating surface BRDF. The numeric experiments performed by Qin et al. (2001) have demonstrated that this method is very robust and accurate. The TOA reflectance can be simulated as

$$\rho^{TOA}(\theta_s,\theta_v,\varphi) = t_{H_2O}\left(\rho_0(\theta_s,\theta_v,\varphi) + \frac{\boldsymbol{T}(\theta_s)\cdot\boldsymbol{R}(\theta_s,\theta_v,\varphi)\cdot\boldsymbol{T}(\theta_v) - t_{dd}(\theta_s)\cdot t_{dd}(\theta_v)\cdot|\boldsymbol{R}(\theta_s,\theta_v,\varphi)|\cdot\overline{\rho}}{1-r_{hh}\overline{\rho}}\right), \tag{16}$$

Table 5
Coefficients for narrow-to-broadband conversions over snow/ice surfaces.

Coefficients	c_0	c_1	c_2	c_3	c_4	c_5	c_6	c_7
The wavelength ranges of MODIS bands (μm)	(Offset)	(0.62–0.67)	(0.84–0.87)	(0.46–0.48)	(0.54–0.56)	(1.23–1.25)	(1.63–1.65)	(2.11–2.15)
Snow/ice	−0.0093	0.1574	0.2789	0.3829	0.0000	0.1131	0.0000	0.0694

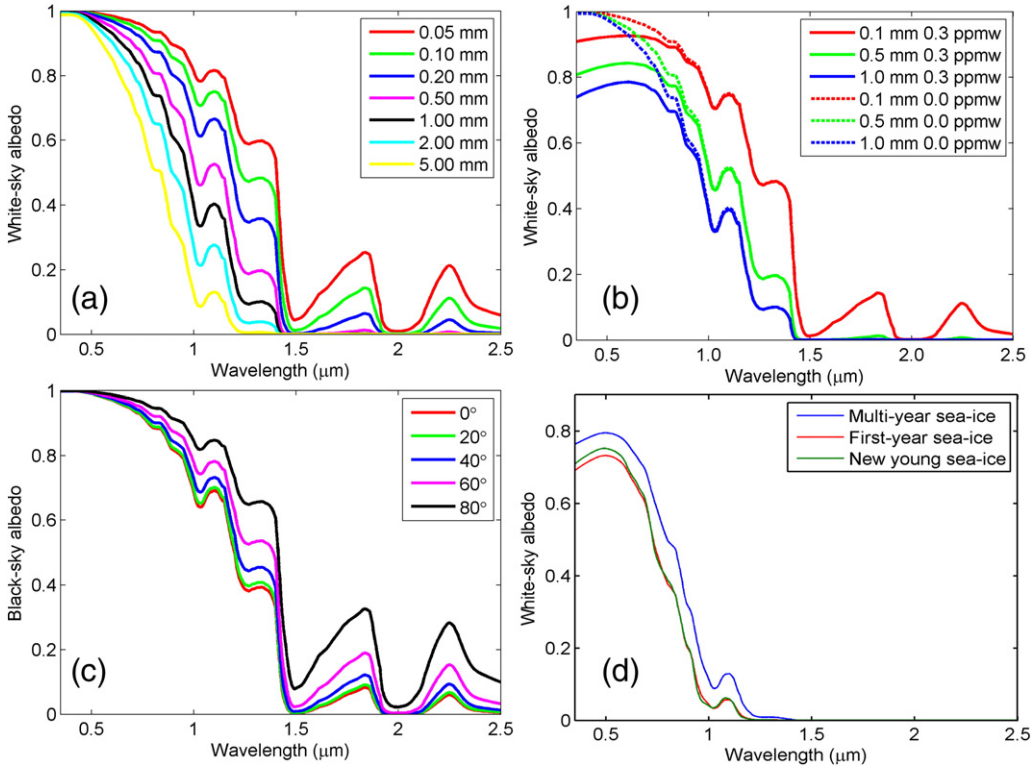

Fig. 5. The dependences of albedo on physical parameters and viewing geometries. (a) The white-sky albedo varies with snow grain size; (b) the white-sky albedo varies with soot concentrations; (c) the black-sky albedo varies with viewing zenith angle; (d) the white-sky albedo varies with sea-ice types (the physical parameters of these sea-ice types are shown in Table 7).

where the matrices $\boldsymbol{T}(\theta_s)$, $\boldsymbol{T}(\theta_v)$, and $\boldsymbol{R}(\theta_s,\theta_v,\varphi)$ are defined as

$$\boldsymbol{T}(\theta_s) = [t_{dd}(\theta_s)\ \ t_{dh}(\theta_s)] \tag{17}$$

$$\boldsymbol{T}(\theta_v) = \begin{bmatrix} t_{dd}(\theta_v) \\ t_{hd}(\theta_v) \end{bmatrix} \tag{18}$$

$$\boldsymbol{R}(\theta_s,\theta_v,\varphi) = \begin{bmatrix} r_{dd}(\theta_s,\theta_v,\varphi) & r_{dh}(\theta_s,\varphi) \\ r_{hd}(\theta_v,\varphi) & r_{hh} \end{bmatrix}, \tag{19}$$

where $\rho^{TOA}(\theta_s,\theta_v,\varphi)$ is the TOA reflectance, $\rho_0(\theta_s,\theta_v,\varphi)$ is the path reflectance of the atmosphere, t_{H_2O} is the transmittance of the water vapor, $\overline{\rho}$ is the downward spherical albedo of the atmosphere (the fraction of ground-level upward flux that been reflected downward by the atmosphere), and where t and r denote transmittance and reflectance, respectively. The subscripts h and d stand for hemispheric (diffuse) and directional (direct), respectively, and the 4 combinations of these 2 symbols *dd*, *dh*, *hd*, and *hh* stand for bi-directional, directional-hemispheric, hemispheric-directional, and bi-hemispheric, respectively.

Thus, $t_{dd}(\theta_s)$ and $t_{dd}(\theta_v)$ are the downward and upward bi-directional path transmittances (BDTs), respectively and $t_{dh}(\theta_s)$ and $t_{hd}(\theta_v)$ are the directional-to-hemispheric path transmittance (DHT) and the hemispheric-to-directional transmittance (HDT), respectively.

$r_{dd}(\theta_s,\theta_v,\varphi)$, $r_{dh}(\theta_s,\varphi_s)$, $r_{hd}(\theta_v,\varphi_v)$, and r_{hh} are the surface bi-directional reflectance (BDR), directional-to-hemispheric reflectance (DHR), hemispheric-to-directional reflectance (HDR) and bi-hemispheric reflectance (BHR), respectively.

The values of reflectance-related parameters ($r_{dh}(\theta_s,\varphi_s)$, $r_{hd}(\theta_v,\varphi_v)$, and r_{hh}) are calculated by the ART and TCOWA model, and the values of atmospheric-related parameters ($\rho_0(\theta_s,\theta_v,\varphi)$, $t_{dh}(\theta_s)$, $t_{hd}(\theta_v)$, $t_{dd}(\theta_s)$, $t_{dd}(\theta_v)$, $\overline{\rho}$, and t_{H_2O}) are obtained from 6S code (Kotchenova et al., 2006) simulations. The input parameters values of the 6S code simulations are listed in Table 6. Arctic summer and winter are selected as the atmospheric types, and continental and maritime are selected as the aerosol types. The aerosol optical depth (AOD) ranges from 0.0 to 0.2 in increments of 0.05, which is consistent with our previous study in the Arctic region (Liang et al., 2005).

2.5. Lambertian-based method and BRDF-based direct-estimation algorithm

When we assume that the land-surface is lambertian (reflectance isotropy), the reflectance at different solar/view angles is identical, and the value of albedo is equal to the reflectance. The broadband surface albedo can be easily estimated by Eq. (13). However, the snow/sea-ice surface is not lambertian but has strong forward scattering effect. Thus, the albedo estimated by the lambertian-based method usually has a large bias depending on the surface conditions and solar/view geometries. In this study, we use this method as the control group for

Table 7
Physical parameters of typical sea-ice cases.

Type	Parameters				
Sea ice	Brine pocket volume fraction	Brine pocket radius (μm)	Air bubble volume fraction	Air bubble radius (μm)	Impurities volume fraction (ppmv)
Multi-year sea-ice	0.1	500	0.05	500	1
First-year sea-ice	0.15	500	0.01	200	1
New young sea-ice	0.25	500	0.01	200	1

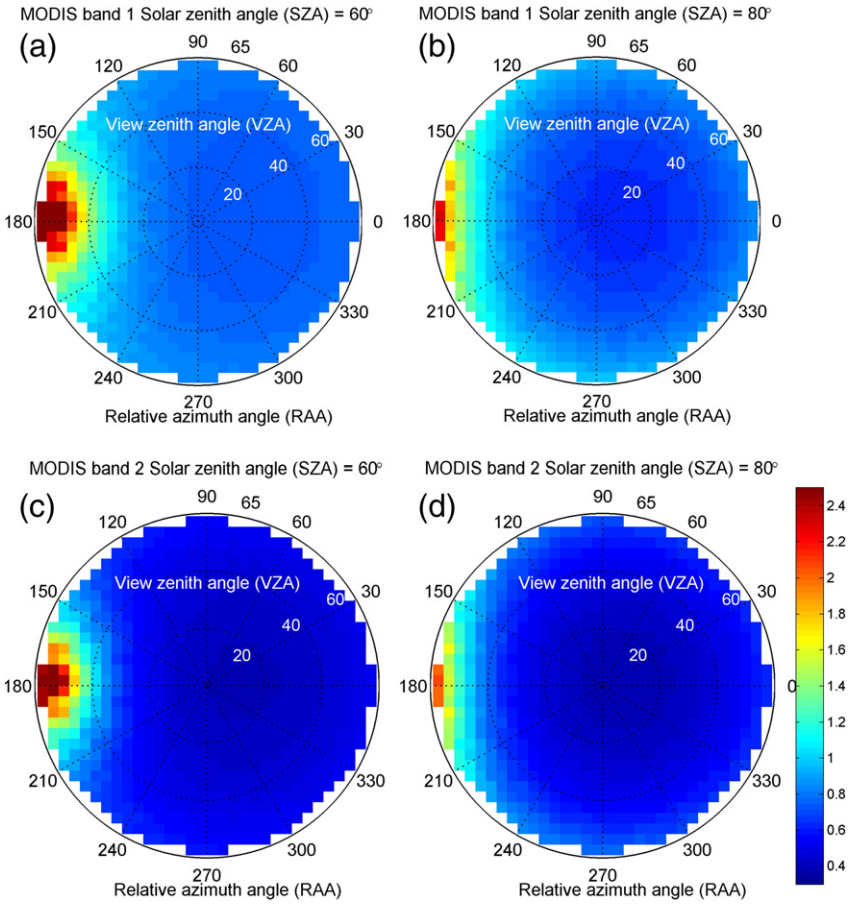

Fig. 6. An example of bare-ice BRDF. Where the surface type is multi-year sea-ice (the physical parameters are shown in Table 7), the radial direction in the polar coordinate stands for the view zenith angle (VZA) (from 0° to 64°), the angle direction stands for the relative azimuth angle (RAA) (from 0° to 360°), and the ramped color stands for the bidirectional reflectance factor (BRF) of MODIS band 1 ((a) and (b)) and 2 ((c) and (d)), respectively; The solar zenith angle is 60° ((a) and (c)) and 80° ((b) and (d)), respectively.

demonstrating the efficiency of the extended BRDF-based direct-estimation algorithm.

When the training dataset (TOA reflectance and its corresponding surface broadband albedo) is obtained by abovementioned steps (BRDF database modeling, broadband albedo estimating and atmospheric radiative transfer simulations), the relationship between TOA reflectance and surface broadband albedo is developed by angular bin regression. Because it is not possible to develop a linear relationship globally, we divide the solar/view geometry into small angular bins, then establish linear regression relationships among different solar/view angles. In this study, a multi-variate linear regression relationship is assumed between the broadband surface albedo and MODIS TOA

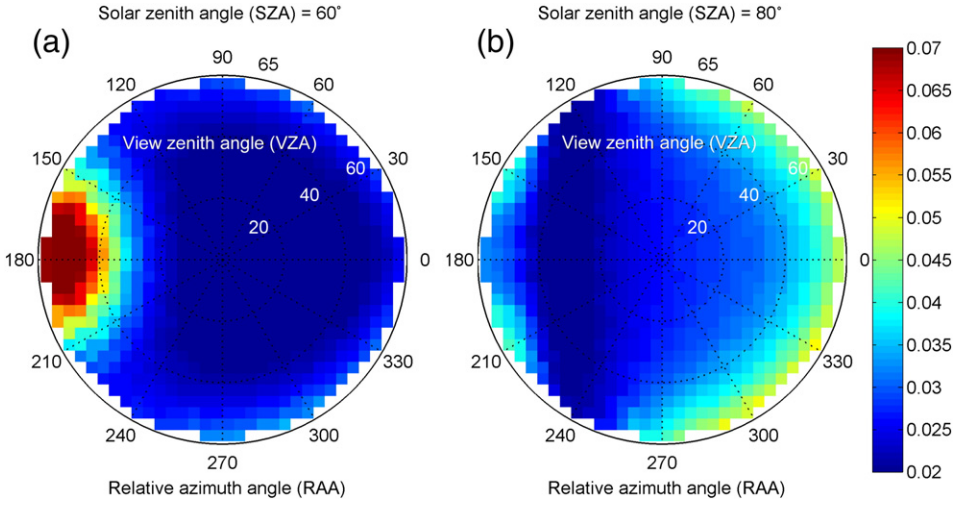

Fig. 7. The angular distribution of uncertainty of the retrieval (in term of RMSE). Where the radial direction in the polar coordinate stands for the view zenith angle (VZA) (from 0° to 64°), the angle direction stands for the relative azimuth angle (RAA) (from 0° to 360°), and the ramped color stands for the retrieval RMSE of each angular bin; The solar zenith angle is 60° (a) and 80° (b), respectively.

reflectance (visible and infrared bands) in different angular bins, which can be expressed as follows (Qu et al., 2014)

$$\alpha_{wsa} = m_0(\theta_s, \theta_v, \varphi) + \sum_{i=1}^{n} m_i(\theta_s, \theta_v, \varphi)\rho_i^{TOA}(\theta_s, \theta_v, \varphi) \quad (20)$$

$$\alpha_{bsa}(\theta_{bsa}) = n_0(\theta_{bsa}, \theta_s, \theta_v, \varphi) + \sum_{i=1}^{n} n_i(\theta_{bsa}, \theta_s, \theta_v, \varphi)\rho_i^{TOA}(\theta_s, \theta_v, \varphi), \quad (21)$$

where α_{wsa} denotes the broadband white-sky albedo, $\alpha_{bsa}(\theta_{bsa})$ denotes the broadband black-sky albedo at SZA of θ_{bsa}, which varies from 0° to 80° in increments of 4° ($\theta_{bsa} = 0, 4, \cdots, 76, 80(°)$), $\rho_i^{TOA}(\theta_s, \theta_v, \varphi)$ is the TOA reflectance of MODIS band i ($i = 1, 2, \cdots, 7$) with SZA of θ_s, VZA of θ_v, and relative azimuth angle of φ; $m_0(\theta_s, \theta_v, \varphi)$ and $n_0(\theta_{bsa}, \theta_s, \theta_v, \varphi)$ are the intersection terms of the regression equations, and $m_i(\theta_s, \theta_v, \varphi)$ and $n_i(\theta_{bsa}, \theta_s, \theta_v, \varphi)$ are the coefficients of the regression equation for each corresponding angular bin. The angular bins are divided as follows: (1) the central SZA of each angular bin varies from 0° to 80° with increments of 2°; (2) the central VZA of each angular bin varies from 0° to 64° with increment of 2°; (3) the central RAA of each angular bin varies from 0° to 180° with increments of 5°. These coefficients of each angular bin are estimated by the least squares method and then stored in the direct-estimation LUT. A sensitivity analysis of the size of angular bin was carried out in the previous study (Qu et al., 2014), however, the angular bins are divided finer than in the previous study, because the hotspots of the snow/sea ice and ocean water BRDF are much narrower than those of land-surfaces.

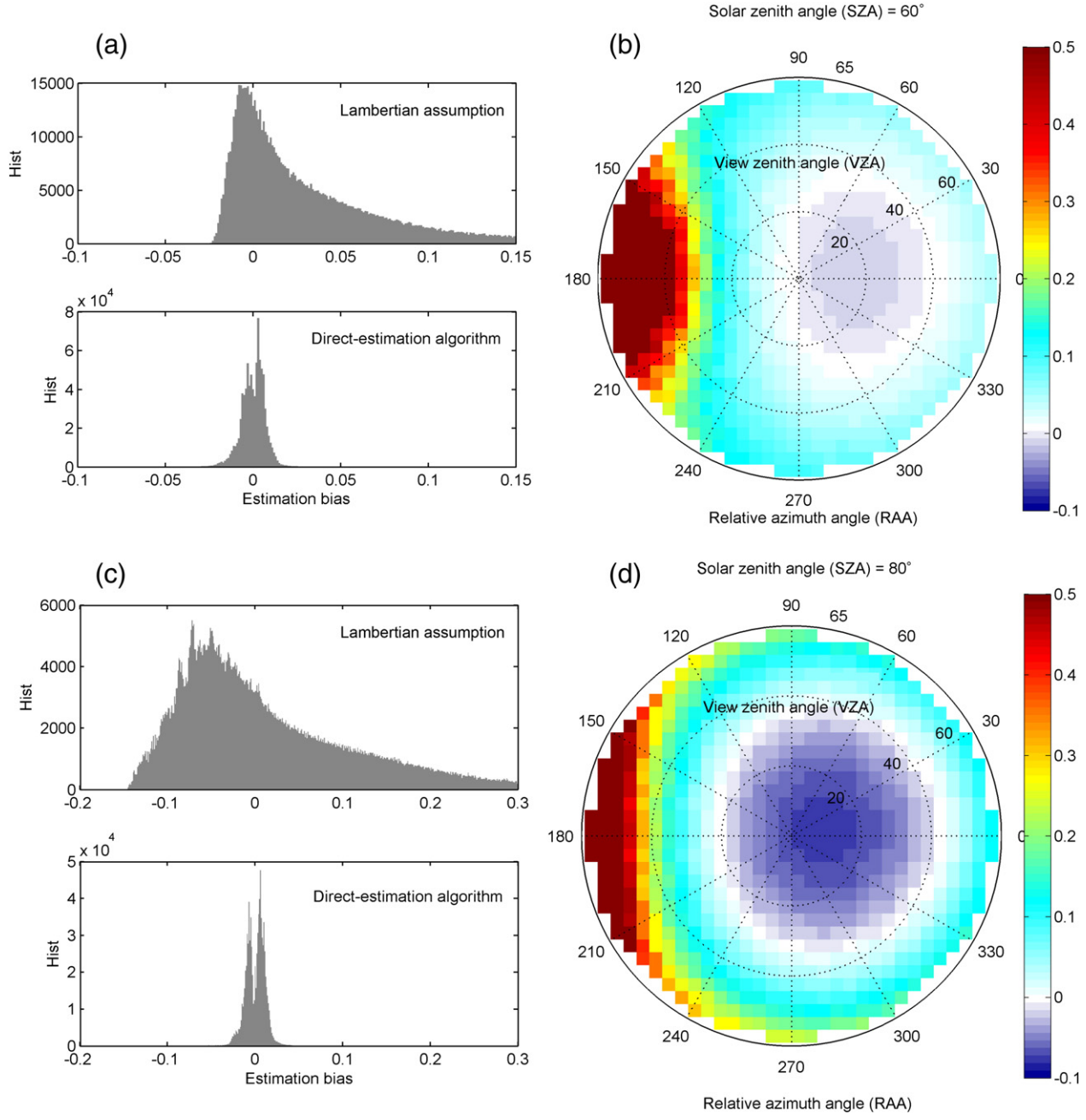

Fig. 8. Comparison of the results estimated by the lambertian-based method and BRDF-based direct-estimation algorithm. Where (a) and (c) are histograms of the estimation bias for the lambertian-based method and BRDF-based direct-estimation algorithm; (b) and (d) are the angular distribution of the estimation bias for the method based on lambertian assumption, where the radial direction in the polar coordinate stands for the view zenith angle (VZA) (from 0° to 64°), the angle direction stands for the relative azimuth angle (RAA) (from 0° to 360°), and the ramped color stands for the mean estimation bias of all samples in each angular bin; where the solar zenith angle (SZA) is 60° ((a) and (b)) and 80° ((c) and (d)), respectively.

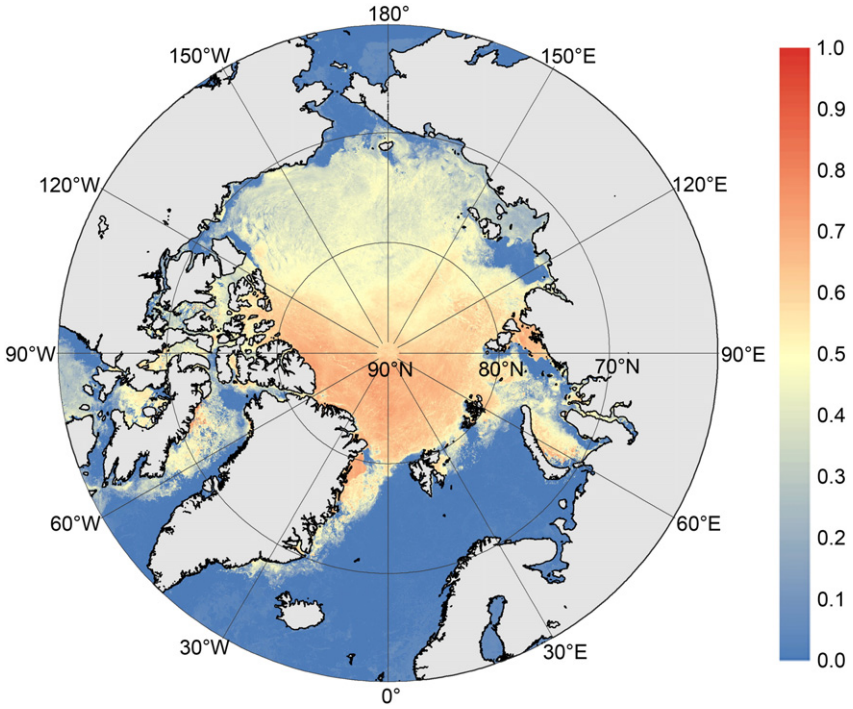

Fig. 9. Shortwave surface albedo map of the Arctic sea-ice zone. White-sky albedo, averaged over a 5 day period from day 166 to day 170 in 2007.

3. Results and discussions

3.1. Representativeness of the snow/sea-ice BRDF/albedo database

In this study, we aimed to build a database which represents different snow/sea-ice types and snow/sea-ice/ocean-water fractions. A surface snow/sea-ice BRDF database is built based on linear combinations of the simulation results of ART and TCOSA models, as well as the POLDER BRDF database. The BRDF/Albedo is simulated by the physical parameters of snow, ice and ocean water surfaces (Tables 2, 3 and 4).

Fig. 5 shows the dependencies of snow/sea-ice albedo on physical parameters and viewing geometries, which is consistent with the results of the published literatures (Gardner and Sharp, 2010; Stamnes et al., 2011). Fig. 5a, b show the dependencies of white-sky albedo on snow grain size (Fig. 5a), and soot concentration (Fig. 5b). Fig. 5c shows the dependencies of black-sky albedo on viewing zenith angle. Fig. 5d shows the white-sky albedo of typical sea-ice cases (multi-year sea-ice, first-year sea-ice and new young sea-ice, where the parameter settings of these sea-ice types are shown in Table 7).

Fig. 6 shows an example of multi-year sea-ice BRDF (the physical parameters are shown in Table 7). At different solar zenith angles and MODIS bands, the sea-ice surface represents strong forward scattering effect. The directional reflectance increases rapidly around the forward direction (when the solar zenith angle equals to the view zenith angle, relative azimuth angle (RAA) is 180°) in the principle plane. Therefore, it is critically necessary to pay attention to the reflectance anisotropic properties and correct this effect to obtain better albedo estimations.

3.2. Accuracy assessments and theoretical error estimations

The uncertainty of the retrieval depends largely on the angular bin regression method, which varies with the solar/view angles and different training dataset. In our former study, the accuracies of the angular bin regression method under different angular bins, aerosol conditions, and land cover types have been extensively evaluated by the POLDER BRDF database, and the results show that it is quite robust at different circumstances (Qu et al., 2014). In this study, a similar assessment is carried out based on the BRDF database built by simulations of physical models. We examined the accuracy dependencies of BRDF based direct-estimation method for different angular bins. For simplicity, the broadband albedos calculated by angular integrating are referred to as "reference albedo", and the broadband albedos calculated by the BRDF based direct-estimation method are referred to as "estimated albedo". The angular distribution of uncertainty of the retrieval (in terms of root mean square error (RMSE)) at solar zenith angles (SZA) of 60° and 80° are shown in Fig. 7. The uncertainty of retrieval (RMSE) ranges from approximately 0.02 to 0.07, and the largest error (approximately 0.07) exists at large view zenith angle (VZA), forward directions (relative azimuth angle (RAA) is 180°). Although the uncertainty of retrieval increases with VZA, the RMSE is quite small and stable over the viewing hemisphere, and the estimations have acceptable accuracy.

3.3. Comparison with the lambertian-based method

In this study, the theoretical estimation accuracy of the BRDF-based direct-estimation algorithm and the lambertian-based method (narrow-to-broadband conversions) are evaluated. Firstly, a validation BRDF dataset (700 samples) is randomly selected from the BRDF database described in Section 2.2 (the BRDF data which has not been selected was used for deriving the direct-estimation coefficients). Then, the shortwave surface albedo is estimated by angular integration, the BRDF-based direct-estimation algorithm and the method based on lambertian assumption. Because the BRDF shape of each sample is determined with very high angular resolutions (2° in solar/view zenith angle, and 5° in relative azimuth angle), the results estimated by angular integration are considered as quite robust and accurate. These results are used as references for evaluating the results estimated by the other two methods. The narrow-to-broadband coefficients provided by (Stroeve et al., 2005) are used for estimating shortwave surface albedo over snow/sea-ice under the lambertian assumption. Finally, the estimation bias (the difference between the estimated results and corresponding "true albedo") are calculated, and the histograms and angular distributions of the estimation bias at solar zenith angles (SZA) of 60° and 80° are shown in Fig. 8.

Fig. 8(a) and (c) show that the histograms from the BRDF-based direct-estimation algorithm have narrower 95% confident intervals

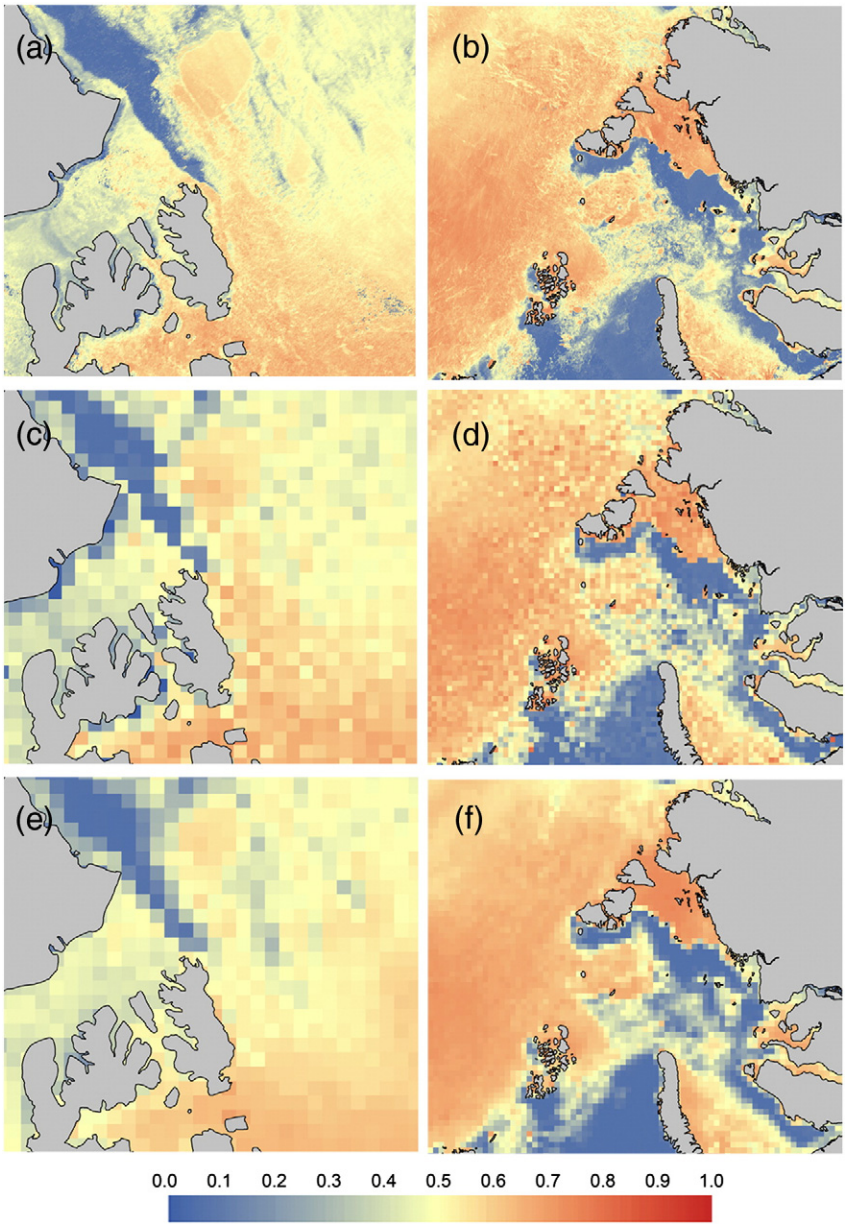

Fig. 10. Partial enlarged views of the Arctic sea-ice albedo map. Shortwave surface albedo (white-sky albedo) averaged over a 5 day period from day 166 to day 170 in 2007; where (a) and (b) are the albedo map derived by the BRDF-based direct-estimation algorithm (1 km), (c) and (d) are the direct-estimated albedo map resampled to 25 km, (e) and (f) are the albedo map derived by the CLARA SAL product (25 km); (a), (c) and (e) are albedo maps around the Banks, Prince Patrick, and Melville Islands; (b), (d) and (f) are albedo maps around the Kara Sea.

(approximately 0.015 to 0.02) than those from the method based on lambertian assumption (approximately 0.15 to 0.3) and unbiased to the theoretical "true albedo". Fig. 8(b) and (d) show that the surface albedo tends to be underestimated by the method based on the lambertian assumption at large SZA (60° to 80°) when the VZA is less than 30° in the backward direction and be overestimated when the VZA is larger than 30°, especially in the forward direction (RAA = 180°). The large biases of the method based on the lambertian assumption at large SZA and VZA are due to the reflectance anisotropic effect of snow/sea-ice, which has a strong forward scattering effect that cannot be ignored. Note that the angular distribution of the estimation bias for the BRDF-based direct-estimation algorithm is not shown, because the mean biases of the BRDF-based direct-estimation algorithm are very close to zero, which means that it is unbiased at different angular bins. This assessment demonstrates that it is necessary to correct for the reflectance anisotropic effect, and the BRDF-based direct-estimation algorithm is a good choice to achieve this purpose.

3.4. Comparison between the direct-estimated albedo and the CLARA SAL product

In this section, a comparison between the direct-estimated albedo and the CLARA SAL product which is derived based on temporal averaging of multi-angular surface reflectance was carried out. The CLARA SAL product is employed as a reference for evaluating the performances of the direct-estimation algorithm. The direct-estimated shortwave surface albedo of the Arctic sea-ice zone is derived by the following steps: (1) convert the MODIS Level 1B (L1B) swath data (TOA reflectance of 7 visible-infrared bands, quality assessment (QA) with cloud mask information, solar/view geometry (SZA, VZA, and RAA), water vapor content and so on) to Equal-Area Scalable Earth Grid (EASE-Grid) North projection with a spatial resolution of 1 km; (2) direct-estimate the instantaneous albedo from cloud-free MODIS L1B reflectance data, where the albedo is estimated by Eqs. (20) and (21); (3) generate a daily albedo product based on averaging the albedo estimated from multi-orbit

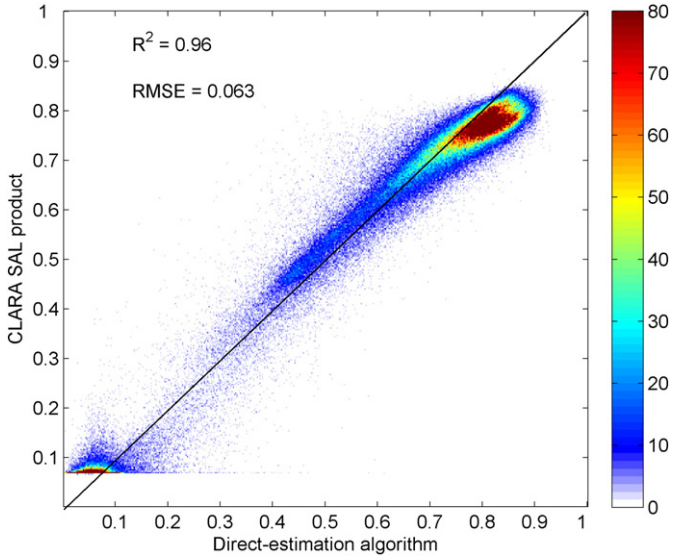

Fig. 11. Comparison of the direct-estimation albedo (white-sky albedo) and CLARA SAL product. Where the ramped color stands for the number of the CLARA SAL-direct estimate albedo pairs fall in each pixel (0.023 × 0.023).

observations during a day, where instantaneous albedos with large fluctuations are excluded; (4) generate a pentad (5 days) albedo product by averaging over a 5 day-period, cloud-free direct-estimated albedo (the pixels which SZA is larger than 80° were masked as invalid pixels). A threshold based pre-classification for sea-ice presence before the albedo estimation. When $r_{b3}>0.1$ (r_{b3} stands for the reflectance of MODIS band 3), the direct-estimation LUT for sea ice is used; when $r_{b3}\leq 0.1$ the direct-estimation LUT for ocean water is used for estimating broadband albedo (The value of 0.076 is used as a filling value for unfrozen ocean water when there are no valid observations).

Fig. 9 shows an example for the shortwave surface albedo of the Arctic sea-ice zone (white-sky albedo, averaged over a 5 day period from day 166 to day 170 in 2007) derived by the BRDF-based direct-estimation algorithm. The Arctic sea ice melts and shrinks in June and moves with the Arctic Ocean current. The shortwave surface albedo decreases rapidly and ranges from approximately 0.4 to 0.7. The albedo of the sea ice on the edge is much lower than that in the polar region, and the albedo of snow-covered multi-year sea-ice region (approximately 0.6–0.7) near the Greenland is relative higher than that of snow-covered first-year sea-ice region (approximately 0.4–0.6) near the East Siberian, Beaufort and Laptev Seas. Fig. 10 shows partially enlarged views of the Arctic shortwave surface albedo map. Fig. 10 (a) and (b) are albedo maps around the Banks, Prince Patrick and Melville Islands; (c) and (d) are albedo maps around the Kara Sea. Because the spatial resolution of the direct-estimated albedo product (1 km) is much finer than the CLARA SAL product (25 km), the direct-estimated albedo product can represent more details of the spatial variations of the Arctic sea-ice, especially on edges of the sea ice cap. The high spatial-resolution albedo map derived in this study shows great advantages and potential abilities for providing more accurate information to surface energy budget models.

Fig. 11 shows the scatter plot of the direct-estimated albedo and the CLARA SAL product, where the ramped color stands for the number of the CLARA SAL-direct estimated albedo pairs fall in each pixel (0.023 × 0.023). From this figure, we can see that most of the scatters cluster around the 1 by 1 line, with an R^2 value of 0.96 and RMSE of 0.063. The biases that occur in high albedo value region (0.8–0.9) are due to different estimation methods (BRDF based direct-estimation algorithm for this study, and the method based on temporal averaging of multi-angular surface reflectance for CLARA SAL product), and the biases that occur in low albedo value region (less than 0.1) are mainly due to neglecting the contributions of whitecaps and sun glint in CLARA SAL product.

3.5. Validation with Tara measurements

The sources of estimation errors in the BRDF based direct-estimation algorithm can be categorized into three parts: (1) the theoretical estimation errors at different solar/view angles; (2) the errors caused by simulations of physical models; (3) the errors caused by sensor noise. The theoretical estimation errors at different solar/view angles have been evaluated in Section 3.2. The other two sources of estimation error can be evaluated based on validations with in situ measurement datasets.

In this study, the BRDF based direct-estimated albedo is validated with in situ meteorological observations carried out by the Tara Oceans Polar Circle expedition (Vihma et al., 2008) of 2007. The Tara drifting ice station crossed the central Arctic Ocean from 23 March to 19 September 2007 (from East Siberia to Greenland), and the route of the Tara polar ocean expedition is shown in Fig. 12. The upward and downward shortwave radiation was measured by a pair of Eppley PSP pyranometers which are mounted on a 10 m-high weather mast with a minimum measured interval of 1 min, as well as meteorological data (temperature, wind speed and humidity).

Fig. 13 shows the Tara in situ measurements (daily-averaged instantaneous albedo), and the corresponding estimations of the BRDF-based direct-estimation algorithm from MODIS data, CLARA SAL product (normalized black-sky albedo product), from the day of 130 to 220 in 2007. In this period, the sea ice drifting in the Arctic Ocean, and the surface albedo decreased from approximately 0.85 to 0.55. Although there are no estimated values for several days due to the clouds obscuration, the temporal characteristics are well captured by the BRDF-based direct-estimation algorithm. Validation studies for albedo in the polar region are easily affected by clouds, shadowing effects, and spatial representativeness of the in situ measurements (Riihelä et al., 2010). With these uncertainties in mind, the estimation results derived by the BRDF-based direct-estimation algorithm are quite consistent with the Tara in situ measured data in most temporal periods. Compared with the CLARA SAL product (5 days), the temporal resolution of direct-estimated albedo (daily) is finer, thus more details of the temporal variations are represented. Fig. 14 shows the scatter plot of the direct-estimated albedo versus the Tara measured data (daily local noon albedo, nearest-neighborhood matching). The comparison results show that the albedo estimated by the BRDF-based direct-estimation algorithm has an R^2 value of 0.67 and RMSE of 0.068, and the CLARA SAL product has an R^2 value of 0.81 and RMSE of 0.097.

3.6. Relationship with sea ice concentration

In this study, the relationships between the direct-estimated surface albedo of sea ice surface and the sea ice concentration are examined. The (National Oceanic and Atmospheric Administration) NOAA/National Snow and Ice Data Center (NSIDC) Climate Data Record (CDR) of passive microwave sea ice concentration data (version 2) (Peng et al., 2013) is used this study. The direct-estimated surface albedo product is aggregated to the same spatial resolution as the sea ice concentration data, and the pixels with cloud obscurations are excluded. Fig. 15 shows a scatter plot of sea ice albedo versus sea ice concentration (fraction). From this figure, we can see that the sea ice concentration is strongly related to the broadband surface albedo; the albedo decreases as the sea ice concentration decreases. The surface albedo has a much larger range of variation when the sea ice concentration approaches 100%, because when the ocean is almost fully covered by sea ice, the surface albedo largely depends on the surface properties of the sea ice and less on the sea-ice covered fraction. The relationship between sea ice surface albedo and sea ice concentration can be regressed by a linear function, with an R^2 value of 0.54 and RMSE of 0.095.

Fig. 12. The Arctic map and route of the Tara polar ocean expedition. Where the route of Tara polar ocean expedition is denoted by the red line, and the sea ice extent at April and September are shown in light and deep blue polygons, respectively. This figure is draw with the aid of the Arctic portal interactive map tool (http://portal.inter-map.com/).

3.7. Discussions of limitations

Although the broadband surface albedo of Arctic sea-ice region can be efficiently estimated by the direct-estimated algorithm, there are still several limitations and potential shortages which need to be improved in the future. The main issues are listed as follows:

(1) The linear combination assumption was used for building the training dataset for considering of the complexity of simulations. This assumption is only acceptable when the spatial resolution of satellite observations is very coarse (>1 km). When the spatial resolution is smaller than 100 m, the depth of snow, sea-ice, and melt ponds should be taken for consideration.

(2) As the training dataset was partially built based on models, the effects of the simplifications of models on the direct-estimation algorithm should be noted. In this study, the ART, TCOWA, and atmospheric radiative transfer models are used for simulating the satellite observations. For considering the complexity of computation, there are several assumptions and simplifications which may results in errors for particular cases. For example, the relationship between wind speed and waviness is different among sea ice as the ice constricts open water movement, and the growth of chlorophyll works differently in the cold Arctic waters. In the future, more complicated physical models should be employed for simulating the training dataset.

(3) The performances of this algorithm when the SZA is larger than 80° should be improved. In this study, the physical models and semi-empirical linear kernel driven model are used for ensuring the estimation as large zenith angles. However, when the solar zenith angle is larger than 80°, the observations of satellites are unreliable due to the low solar radiation and obscure of clouds. For deriving a robust and reliable broadband surface albedo product, we choose to mask the pixels which SZA is larger than 80°.

(4) A filling and filtering algorithm should be used for deriving a long-term, gap-free surface broadband albedo product. It has been reported that the direct-estimated results are easily affected by the sensor noises and cloud detection error due to it is based on single-angular observation. In this study, the Statistics-based Temporal Filter (STF) (Liu et al., 2013a) was used

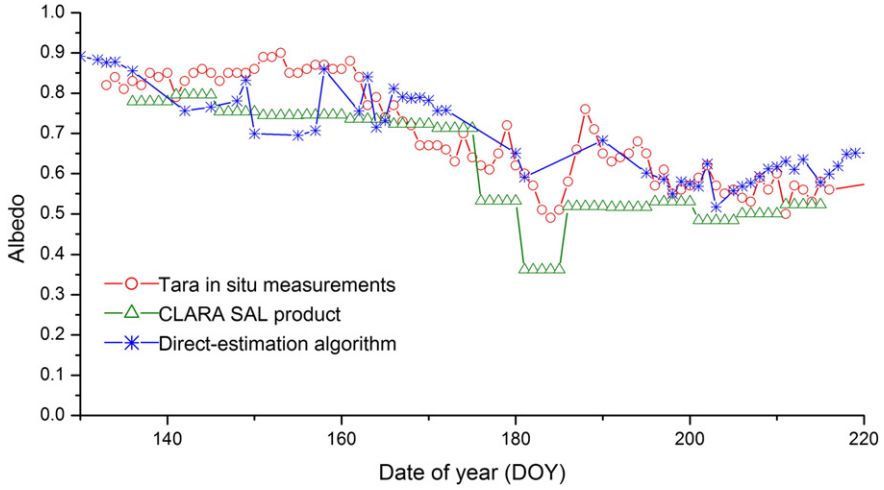

Fig. 13. Comparison of the direct-estimated albedo and Tara in situ measurements. Where the red circles stand for the Tara in situ measurements, the blue asterisks stand for the direct-estimated albedo, and the green triangles stand for the CLARA SAL product.

for obtaining high temporal, gap-free broadband albedo product.

4. Conclusions

The shortwave surface albedo of the Arctic sea ice zone changes rapidly with the seasonal freeze/melts of Arctic sea ice, and long-term broadband surface albedo products over sea-ice surfaces with higher spatial and temporal resolution are required for global climate change studies. This paper extended the BRDF-based direct-estimation algorithm to map shortwave surface albedo of the Arctic sea-ice zone from MODIS data. The results are validated with in situ measurements of the Tara oceans polar circle expedition in 2007, which shows that the albedo estimated by the BRDF-based direct-estimation algorithm has an R^2 value of 0.67 and RMSE of 0.068 and is more accurate than the results estimated by the lambertian-based method.

The following conclusions are made from this study:

(1) The extended BRDF-based direct-estimation algorithm can accurately map ocean albedo at an improved temporal and spatial resolution over the Arctic sea-ice zone. Compared with the algorithms based on multiple-angular observations, the BRDF-based direct-estimation algorithm enables estimates of the broadband surface albedo with only single-angular observation, which can provide higher temporal resolution of Arctic surface albedo. The broadband surface albedo product with finer spatial and temporal resolution can represent much more detailed spatial and temporal characteristics of the Arctic sea-ice zone.

(2) The reflectance anisotropic effect of Arctic sea ice has been effectively corrected based on a prior BRDF database generated by physical BRDF models of snow/ice and ocean waters. In this study, the prior BRDF database for sea ice is built based on ART and TCOWA model, which makes it possible to correct the reflectance anisotropic effect over the sea-ice surface.

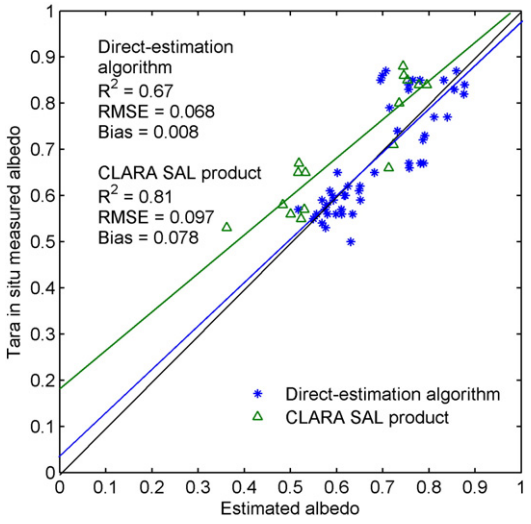

Fig. 14. Scatter plot of the direct-estimated albedo and Tara in situ measurements. Where the blue asterisks stand for the albedo estimated by the BRDF-based direct-estimation algorithm, and the green triangles stand for the CLARA SAL product.

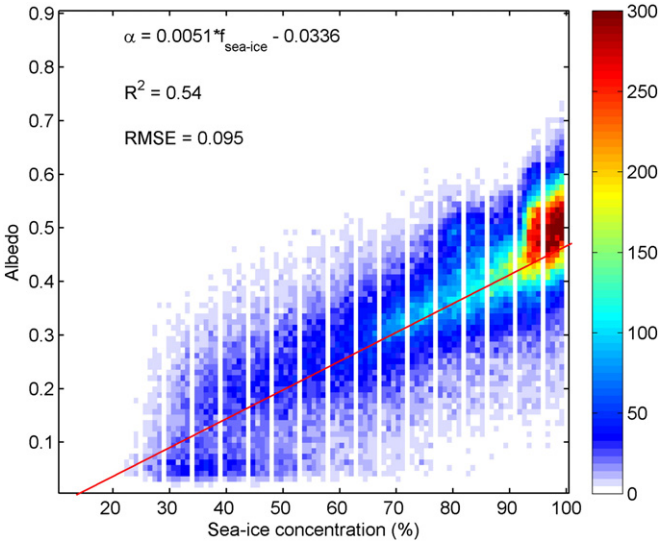

Fig. 15. The relationship between surface albedo (white-sky albedo) and sea-ice concentration. Where the ramped color stands for the number of the scatters fall in each pixel (1 × 0.01).

(3) The broadband surface albedo generated by the direct-estimated algorithm is highly related to the sea ice concentration derived from passive microwave data. A relationship between derived surface albedo and sea ice concentration has been established with an R^2 value of 0.54 and RMSE of 0.095.

This study is part of the efforts for generating a Global Land Surface Satellite (GLASS) product (Liang et al., 2013). In the phase-1 of the GLASS product, a 30-year global surface broadband albedo product (Liu et al., 2013b) has been generated from AVHRR and MODIS data, with spatial resolutions of 1 km and 0.05° and a temporal resolution of 8 days. However, it covers land-surface only, and the surfaces over ocean water and sea ice are left blank. In the phase-2 of the GLASS product, the BRDF-based direct-estimation algorithm for mapping Arctic sea-ice albedo is employed, and a long-term, gap-free, global fully covered (including land, ocean, and sea ice surfaces) surface albedo product will be released on websites of the Beijing Normal University Center for Global Change Data Processing and Analysis (www.bnu-datacenter.com) and the University of Maryland Global Land Cover Facility (glcf.umd.edu).

Acknowledgements

The authors would like to thank Timo Palo, Erko Jakobson and Jaak Jaagus from the University of Tartu, Estonia, for providing the Tara in situ measured radiation data. This research was financially supported by the Fundamental Research Funds for the Central Universities (2412016KJ028), the Open Funds of State Key Laboratory of Remote Sensing Science (OFSLRSS201624), the "State Program for High-Tech Research and Development (863 program)" (2013AA122801), the China Postdoctoral Science Foundation (2014M550025), and the National Natural Science Foundation of China (41371356). We are grateful to anonymous reviewers for their valuable comments and suggestions, which greatly improve the presentation of this paper.

References

Bourgeois, C., Calanca, P., Ohmura, A., 2006. A field study of the hemispherical directional reflectance factor and spectral albedo of dry snow. J. Geophys. Res. - Atmos. 111, D20108.
Cao, Y., Liang, S., Chen, X., He, T., 2015. Assessment of sea-ice albedo radiative forcing and feedback over the Northern Hemisphere from 1982 to 2009 using satellite and reanalysis data. J. Climate 28, 1248–1259.
Comiso, J.C., 2001. Satellite-observed variability and trend in sea-ice extent, surface temperature, albedo and clouds in the Arctic. Ann. Glaciol. 33, 457–473.
Cox, C., Munk, W., 1954. Measurement of the roughness of the sea surface from photographs of the sun's glitter. J. Opt. Soc. Am. 44, 838–850.
Curry, J.A., Schramm, J.L., Ebert, E.E., 1995. Sea ice-albedo climate feedback mechanism. J. Clim. 8, 240–247.
De Abreu, R., Key, J., Maslanik, J., Serreze, M., LeDrew, E., 1994. Comparison of in situ and AVHRR-derived broadband albedo over Arctic sea ice. Arctic 47, 288–297.
Dumont, M., Brissaud, O., Picard, G., Schmitt, B., Gallet, J.-C., Arnaud, Y., 2010. High-accuracy measurements of snow bidirectional reflectance distribution function at visible and NIR wavelengths-comparison with modelling results. Atmos. Chem. Phys. 10, 2507–2520.
Feng, Y., Liu, Q., Qu, Y., Liang, S., 2016. Estimation of the ocean water albedo from remote sensing and meteorological reanalysis data. IEEE Trans. Geosci. Remote Sens. 54, 850–868.
Fyfe, J., Boer, G., Flato, G., 1999. The Arctic and Antarctic Oscillations and their projected changes under global warming. Geophys. Res. Lett. 26, 1601–1604.
Gardner, A.S., Sharp, M.J., 2010. A review of snow and ice albedo and the development of a new physically based broadband albedo parameterization. J. Geophys. Res. Earth Surf. 115, F01009. http://dx.doi.org/10.01029/02009JF001444.
Hall, A., 2004. The role of surface albedo feedback in climate. J. Climate 17, 1550–1568.
Hall, A., Qu, X., 2006. Using the current seasonal cycle to constrain snow albedo feedback in future climate change. Geophys. Res. Lett. 33, L03502.
Hamre, B., Winther, J.-G., Gerland, S., Stamnes, J.J., Stamnes, K., 2004. Modeled and measured optical transmittance of snow-covered first-year sea ice in Kongsfjorden, Svalbard. J. Geophys. Res. 109, C10006.
He, T., Liang, S., Wang, D., Wu, H., Yu, Y., Wang, J., 2012. Estimation of surface albedo and directional reflectance from Moderate Resolution Imaging Spectroradiometer (MODIS) observations. Remote Sens. Environ. 119, 286–300.
He, T., Liang, S., Song, D., 2014. Analysis of global land surface albedo climatology and spatial-temporal variation during 1981–2010 from multiple satellite products. J. Geophys. Res. - Atmos. 119, 10281–10298.
Johannessen, O.M., Bengtsson, L., Miles, M.W., Kuzmina, S.I., Semenov, V.A., Alekseev, G.V., Nagurnyi, A.P., Zakharov, V.F., Bobylev, L.P., Pettersson, L.H., 2004. Arctic climate change: observed and modelled temperature and sea-ice variability. Tellus A 56, 328–341.
Key, J.R., Wang, X., Stoeve, J.C., Fowler, C., 2001. Estimating the cloudy-sky albedo of sea ice and snow from space. J. Geophys. Res. - Atmos. 106, 12489–12497.
Key, J., Wang, X., Liu, Y., 2014. NOAA Climate Data Record of AVHRR Polar Pathfinder Extended (APP-X), Version 1.0. Revision 1. NOAA National Climatic Data Center http://dx.doi.org/10.7289/V5MK69W6.
Knap, W.H., Oerlemans, J., 1996. The surface albedo of the Greenland ice sheet: satellite-derived and in situ measurements in the Søndre Strømfjord area during the 1991 melt season. J. Glaciol. 42, 364–374.
Koepke, P., 1984. Effective reflectance of oceanic whitecaps. Appl. Opt. 23, 1816–1824.
Kokhanovsky, A., Zege, E., 1997. Optical properties of aerosol particles: a review of approximate analytical solutions. J. Aerosol Sci. 28, 1–21.
Kokhanovsky, A.A., Zege, E.P., 2004. Scattering optics of snow. Appl. Opt. 43, 1589–1602.
Kokhanovsky, A.A., Aoki, T., Hachikubo, A., Hori, M., Zege, E.P., 2005. Reflective properties of natural snow: approximate asymptotic theory versus in situ measurements. IEEE Trans. Geosci. Remote Sens. 43, 1529–1535.
Kotchenova, S.Y., Vermote, E.F., Matarrese, R., Klemm Jr., F.J., 2006. Validation of a vector version of the 6S radiative transfer code for atmospheric correction of satellite data. Part I: path radiance. Appl. Opt. 45, 6762–6774.
Kwok, R., Rothrock, D., 2009. Decline in Arctic sea ice thickness from submarine and ICES at records: 1958–2008. Geophys. Res. Lett. 36, L15501.
Laine, V., 2004. Arctic sea ice regional albedo variability and trends, 1982–1998. J. Geophys. Res. Oceans 109, C06027.
Laine, V., Manninen, T., Riihelä, A., Andersson, K., 2011. Shortwave broadband black-sky surface albedo estimation for Arctic sea ice using passive microwave radiometer data. J. Geophys. Res. 116, D16124.
Laine, V., Manninen, T., Riihelä, A., 2014. High temporal resolution estimations of the Arctic sea ice albedo during the melting and refreezing periods of the years 2011. Remote Sens. Environ. 140, 604–613.
Leroy, M., Deuzé, J., Bréon, F., Hautecoeur, O., Herman, M., Buriez, J., Tanré, D., Bouffies, S., Chazette, P., Roujean, J., 1997. Retrieval of atmospheric properties and surface bidirectional reflectances over land from POLDER/ADEOS. J. Geophys. Res. 102, 17023–17037.
Lewis, P., Barnsley, M., 1994. Influence of the sky radiance distribution on various formulations of the earth surface albedo. 6th International Symposium on Physical Measurements and Signatures in Remote Sensing, ISPRS, pp. 707–715.
Liang, S., 2001. Narrowband to broadband conversions of land surface albedo I: algorithms. Remote Sens. Environ. 76, 213–238.
Liang, S., 2003. A direct algorithm for estimating land surface broadband albedos from MODIS imagery. IEEE Trans. Geosci. Remote Sens. 41, 136–145.
Liang, S., Strahler, A., Walthall, C., 1999. Retrieval of land surface albedo from satellite observations: a simulation study. J. Appl. Meteorol. 38, 712–725.
Liang, S., Stroeve, J., Box, J., 2005. Mapping daily snow/ice shortwave broadband albedo from Moderate Resolution Imaging Spectroradiometer (MODIS): the improved direct retrieval algorithm and validation with Greenland in situ measurement. J. Geophys. Res. 110, D10109.
Liang, S., Wang, K., Zhang, X., Wild, M., 2010. Review on estimation of land surface radiation and energy budgets from ground measurement, remote sensing and model simulations. IEEE Journal of Special Topics in Applied Earth Observations and Remote Sensing 3, 225–240.
Liang, S., Zhao, X., Yuan, W., Liu, S., Cheng, X., Xiao, Z., Zhang, X., Liu, Q., Cheng, J., Tang, H., Qu, Y.H., Bai, Y., Qu, Y., Ren, H., Yu, K., Townshend, J., 2013. A long-term Global LAnd Surface Satellite (GLASS) dataset for environmental studies. Int. J. Digital Earth 6 (Suppl. 1), 69–95.
Lindsay, R., Rothrock, D., 1994. Arctic sea ice albedo from AVHRR. J. Clim. 7, 1737–1749.
Liu, J., Zhang, Z., Inoue, J., Horton, R.M., 2007. Evaluation of snow/ice albedo parameterizations and their impacts on sea ice simulations. Int. J. Climatol. 27, 81–91.
Liu, N., Liu, Q., Wang, L., Liang, S., Wen, J., Qu, Y., Liu, S., 2013a. A statistics-based temporal filter algorithm to map spatiotemporally continuous shortwave albedo from MODIS data. Hydrol. Earth Syst. Sci. 17, 2121–2129.
Liu, Q., Wang, L., Qu, Y., Liu, N., Tang, H., Liang, S., Liu, S., 2013b. Preliminary evaluation of the long-term GLASS albedo product. International Journal of Digital Earth 6 (Suppl. 1), 5–33.
Lucht, W., Schaaf, C., Strahler, A., 2000. An algorithm for the retrieval of albedo from space using semiempirical BRDF models. IEEE Trans. Geosci. Remote Sens. 38, 977–998.
Monahan, E.C., Muircheartaigh, I., 1980. Optimal power-law description of oceanic whitecap coverage dependence on wind speed. J. Phys. Oceanogr. 10, 2094–2099.
Morel, A., Maritorena, S., 2001. Bio-optical properties of oceanic waters: a reappraisal. Journal of Geophysical Research: Oceans 106, 7163–7180.
Morel, A., Antoine, D., Gentili, B., 2002. Bidirectional reflectance of oceanic waters: accounting for Raman emission and varying particle scattering phase function. Appl. Opt. 41, 6289–6306.
Pedersen, C.A., 2007. Optical Properties of Snow and Sea Ice: Field Measurements, Parameterization Schemes and Validation. University of Tromsø.
Peltoniemi, J.I., Kaasalainen, S., Naranen, J., Matikainen, L., Piironen, J., 2005. Measurement of directional and spectral signatures of light reflectance by snow. IEEE Trans. Geosci. Remote Sens. 43, 2294–2304.
Peng, G., Meier, W., Scott, D., Savoie, M., 2013. A long-term and reproducible passive microwave sea ice concentration data record for climate studies and monitoring. Earth Syst. Sci. Data 5, 311–318.

Perovich, D., Grenfell, T., Light, B., Hobbs, P., 2002. Seasonal evolution of the albedo of multiyear Arctic sea ice. J. Geophys. Res. 107, 8044.
Perovich, D.K., Light, B., Eicken, H., Jones, K.F., Runciman, K., Nghiem, S.V., 2007. Increasing solar heating of the Arctic Ocean and adjacent seas, 1979–2005: attribution and role in the ice-albedo feedback. Geophys. Res. Lett. 34, L19505.
Pinty, B., Verstraete, M., Gobron, N., Taberner, M., Widlowski, J., Lattanzio, A., Martonchik, J., Dickinson, R., Govaerts, Y., 2005. Coupling diffuse sky radiation and surface albedo. J. Atmos. Sci. 62, 2580–2591.
Post, D.M., Palkovacs, E.P., 2009. Eco-evolutionary feedbacks in community and ecosystem ecology: interactions between the ecological theatre and the evolutionary play. Philos. Trans. R. Soc., B 364, 1629–1640.
Qin, W., Herman, J., Ahmad, Z., 2001. A fast, accurate algorithm to account for non-Lambertian surface effects on TOA radiance. J. Geophys. Res. 106, 22671–22684.
Qu, Y., Liu, Q., Liang, S., Wang, L., Liu, N., Liu, S., 2014. Direct-estimation algorithm for mapping daily land-surface broadband albedo from MODIS data. IEEE Trans. Geosci. Remote Sens. 52, 907–919.
Qu, Y., Liang, S., Liu, Q., He, T., Feng, Y., Liu, S., 2015. Mapping surface broadband albedo from satellite observations: a review of literatures on algorithms and products. Remote Sens. 7, 990–1020.
Riihelä, A., Laine, V., Manninen, T., Palo, T., Vihma, T., 2010. Validation of the Climate-SAF surface broadband albedo product: comparisons with in situ observations over Greenland and the ice-covered Arctic Ocean. Remote Sens. Environ. 114, 2779–2790.
Riihelä, A., Manninen, T., Laine, V., 2013a. Observed changes in the albedo of the Arctic sea-ice zone for the period 1982–2009. Nat. Clim. Chang. 3, 895–898.
Riihelä, A., Manninen, T., Laine, V., Andersson, K., Kaspar, F., 2013b. CLARA-SAL: a global 28 yr timeseries of Earth's black-sky surface albedo. Atmos. Chem. Phys. 13, 3743–3762.
Román, M.O., Schaaf, C.B., Lewis, P., Gao, F., Anderson, G.P., Privette, J.L., Strahler, A.H., Woodcock, C.E., Barnsley, M., 2010. Assessing the coupling between surface albedo derived from MODIS and the fraction of diffuse skylight over spatially-characterized landscapes. Remote Sens. Environ. 114, 738–760.
Sayer, A., Thomas, G., Grainger, R., 2010. A sea surface reflectance model for (A) ATSR, and application to aerosol retrievals. Atmos. Meas. Tech. 3.
Schaaf, C., Gao, F., Strahler, A., Lucht, W., Li, X., Tsang, T., Strugnell, N., Zhang, X., Jin, Y., Muller, J., 2002. First operational BRDF, albedo nadir reflectance products from MODIS. Remote Sens. Environ. 83, 135–148.
Serreze, M.C., Holland, M.M., Stroeve, J., 2007. Perspectives on the Arctic's shrinking sea-ice cover. Science 315, 1533–1536.
Stamnes, K., Tsay, S., Wiscombe, W., Jayaweera, K., 1988. Numerically stable algorithm for discrete-ordinate-method radiative transfer in multiple scattering and emitting layered media. Appl. Opt. 27, 2502–2509.
Stamnes, K., Hamre, B., Stamnes, J.J., Ryzhikov, G., Biryulina, M., Mahoney, R., Hauss, B., Sei, A., 2011. Modeling of radiation transport in coupled atmosphere-snow-ice-ocean systems. J. Quant. Spectrosc. Radiat. Transf. 112, 714–726.
Stokes, G.M., Schwartz, S.E., 1994. The Atmospheric Radiation Measurement (ARM) Program: programmatic background and design of the cloud and radiation test bed. Bull. Am. Meteorol. Soc. 75, 1201–1221.
Strahler, A., Muller, J., Lucht, W., Schaaf, C., Tsang, T., Gao, F., Li, X., Lewis, P., Barnsley, M., 1999. MODIS BRDF/albedo product: algorithm theoretical basis document version 5.0. MODIS Documentation.
Stroeve, J., Nolin, A., Steffen, K., 1997. Comparison of AVHRR-derived and in situ surface albedo over the Greenland ice sheet. Remote Sens. Environ. 62, 262–276.
Stroeve, J.C., Box, J.E., Fowler, C., Haran, T., Key, J., 2001. Intercomparison between in situ and AVHRR polar pathfinder-derived surface albedo over Greenland. Remote Sens. Environ. 75, 360–374.
Stroeve, J., Box, J., Gao, F., Liang, S., Nolin, A., Schaaf, C., 2005. Accuracy assessment of the MODIS 16-day albedo product for snow: comparisons with Greenland in situ measurements. Remote Sens. Environ. 94, 46–60.
Stroeve, J., Holland, M.M., Meier, W., Scambos, T., Serreze, M., 2007. Arctic sea ice decline: faster than forecast. Geophys. Res. Lett. 34, L09501.
Stroeve, J.C., Kattsov, V., Barrett, A., Serreze, M., Pavlova, T., Holland, M., Meier, W.N., 2012. Trends in Arctic sea ice extent from CMIP5, CMIP3 and observations. Geophys. Res. Lett. 39, L16502.
Trenberth, K.E., Fasullo, J.T., Kiehl, J., 2009. Earth's global energy budget. Bull. Am. Meteorol. Soc. 90, 311–323.
Vihma, T., Jaagus, J., Jakobson, E., Palo, T., 2008. Meteorological conditions in the Arctic Ocean in spring and summer 2007 as recorded on the drifting ice station Tara. Geophys. Res. Lett. 35, L18706. http://dx.doi.org/10.11029/12008GL034681.
Wang, X., Key, J.R., 2005. Arctic surface, cloud, and radiation properties based on the AVHRR Polar Pathfinder dataset. Part I: spatial and temporal characteristics. J. Clim. 18, 2558–2574.
Wang, D., Liang, S., He, T., Yu, Y., 2013. Direct estimation of land surface albedo from VIIRS data: algorithm improvement and preliminary validation. J. Geophys. Res. - Atmos. 118, 12577–12586.
Wu, H., Liang, S., Tong, L., He, T., Yu, Y., 2012. Bidirectional reflectance for multiple snow-covered land types from MISR products. IEEE Geosci. Remote Sens. Lett. 9, 994–998.
Xiong, X., Stamnes, K., Lubin, D., 2002. Surface albedo over the Arctic Ocean derived from AVHRR and its validation with SHEBA data. J. Appl. Meteorol. 41, 413–425.
Zege, E., Katsev, I., Malinka, A., Prikhach, A., Heygster, G., Wiebe, H., 2011. Algorithm for retrieval of the effective snow grain size and pollution amount from satellite measurements. Remote Sens. Environ. 115, 2674–2685.